Phys Chem Minerals (2016) 43:315–326
DOI 10.1007/s00269-015-0796-z

ORIGINAL PAPER

Thermal equation of state of natural tourmaline at high pressure and temperature

Jingui Xu[1,2] · Yunqian Kuang[1,2] · Bo Zhang[1,2] · Yonggang Liu[1] · Dawei Fan[1,3] · Xiaodong Li[4] · Hongsen Xie[1]

Received: 11 October 2015 / Accepted: 18 December 2015 / Published online: 12 January 2016

Abstract Synchrotron-based in situ angle-dispersive X-ray diffraction experiments were conducted on a natural uvite-dominated tourmaline sample by using an external-heating diamond anvil cell at simultaneously high pressures and temperatures up to 18 GPa and 723 K, respectively. The angle-dispersive X-ray diffraction data reveal no indication of a structural phase transition over the P–T range of the current experiment in this study. The pressure–volume–temperature data were fitted by the high-temperature Birch–Murnaghan equation of state. Isothermal bulk modulus of $K_0 = 96.6$ (9) GPa, pressure derivative of the bulk modulus of $K_0' = 12.5$ (4), thermal expansion coefficient of $\alpha_0 = 4.39$ (27) $\times 10^{-5}$ K^{-1} and temperature derivative of the bulk modulus $(\partial K/\partial T)_P = -0.009$ (6) GPa K^{-1} were obtained. The axial thermoelastic properties were also obtained with $K_{a0} = 139$ (2) GPa, $K_{a0}' = 11.5$ (7) and $\alpha_{a0} = 1.00$ (11) $\times 10^{-5}$ K^{-1} for the a-axis, and $K_{c0} = 59$ (1) GPa, $K_{c0}' = 11.4$ (5) and $\alpha_{c0} = 2.41$ (24) $\times 10^{-5}$ K^{-1} for the c-axis. Both of axial compression and thermal expansion exhibit large anisotropic behavior. Thermoelastic parameters of tourmaline in this study were also compared with that of the other two ring silicates of beryl and cordierite.

Keywords Equation of state · Tourmaline · Diamond anvil cell · High-temperature and high-pressure · X-ray diffraction

Introduction

Tourmaline is the term of a supergroup which covering several closely related minerals rather than a single mineral (Henry et al. 2011). This group of minerals has a complex general chemical formula with $XY_3Z_6[T_6O_{18}][BO_3]_3V_3W$, where $X = K^+$, Na^+, Ca^{2+}, Pb^{2+}, vacancy, $Y = Li^+$, Mg^{2+}, Ti^{4+}, Al^{3+}, Mn^{3+}, Cr^{3+}, V^{3+}, Fe^{3+}, Fe^{2+}, Mn^{2+}, Cu^{2+}, $Z = Mg^{2+}$, Fe^{2+}, Fe^{3+}, V^{3+}, Cr^{3+}, Al^{3+}, $T = Si^{4+}$, B^{3+}, Al^{3+}, $B = B^{3+}$, $V = OH^-$, O^{2-} and $W = O^{2-}$, F^-, OH^- (Hawthorne and Dirlam 2011). Recently, Wunder et al. (2015) found that the X site can also be occupied by $[NH_4]^+$ in their synthetic ammonium-bearing tourmaline. Tourmaline has a trigonal crystal system with space group of $R3m$ (Fig. 1), the cyclosilicate structure is formed by six corner-shared TO_4 tetrahedra, and the T site is mainly occupied by Si, although the substitutions of B (e.g., Hughes et al. 2000; Schreyer et al. 2000) and Al (Rosenberg and Foit 1979) for Si exist. In addition, boron occupies the triangularly coordinated B site. Meanwhile, the Y and Z sites are both octahedrally coordinated and the X site is nine-coordinated. Tourmaline has been widely used in many areas. For instance, fantastic colors and hardness make it a spectacular gemstone. Its other physical properties such as pyroelectricity and piezoelectricity can be used in the manufacture of pressure gauges and other electronic components (Nesse 2000).

✉ Dawei Fan
fandawei@vip.gyig.ac.cn

1 Key Laboratory of High Temperature and High Pressure Study of the Earth's Interior, Institute of Geochemistry, Chinese Academy of Sciences, Guiyang 550081, China

2 University of Chinese Academy of Sciences, Beijing 100049, China

3 Center for High Pressure Science and Technology Advanced Research, Changchun 130012, China

4 Beijing Synchrotron Radiation Facility, Institute of High Energy Physics, Chinese Academy of Sciences, Beijing 100049, China

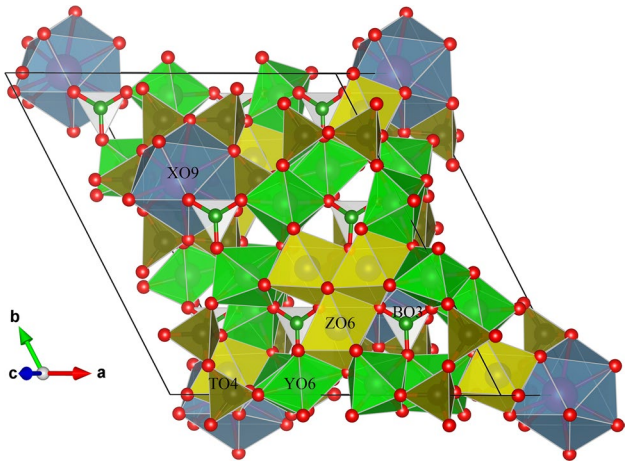

Fig. 1 Crystal structure of tourmaline. (*Color online*)

Tourmaline also plays an important role in geosciences. It can exist in igneous rocks (usually in highly chemical fractionated rocks such as granitic pegmatites, granite and granodiorite), sedimentary rocks (its high resistance during weathering makes it a clastic component in sediment) and metamorphic rocks (commonly formed from preexisting tourmaline detrital grains and diagenetic cores) as a minor or accessory mineral (van Hinsberg et al. 2011a). It also is known as a major mineral in tourmalinites (Slack 1996). Its complexity in composition gives the geological history information of incomparably large range of different elements (Marschall and Jiang 2011), since element diffusion in its structure is negligible (van Hinsberg et al. 2011b), and it is stable over a wide pressure and temperature range from near surface (Henry et al. 1999) to mantle conditions (Krosse 1995; Ota et al. 2008a; Marschall et al. 2009). Since tourmaline is extensively existed in many hydrothermal ore deposits such as mesothermal gold, sulfide and uranium deposits (Slack and Trumbull 2011), the isotope systematic of tourmaline is widely used to identify likely fluid sources for ore genesis (e.g., Palmer and Slack 1989; Taylor et al. 1992, 1999; Jiang et al. 2002). In addition, due to its slow volume diffusion (Henry and Dutrow 1996; Desbois and Ingrin 2007), large grain size and recognizable growth zones (Marschall and Jiang 2011), tourmaline is also a utility isotopic clock in geochronology.

It is generally believed that the components from the slab are probably brought by fluids to the mantle wedge in deep subduction zones, which induce partial melting and the forming of island arc magmas (e.g., Perfit et al. 1980; Saunders et al. 1980; Nakamura et al. 1985). Therefore, to investigate the nature of the subducting slabs is significant for understanding the crust–mantle recycling in subduction zones (Moriguti et al. 2004). The light elements lithium and boron are widely used as the important geochemical tracers for crust–mantle recycling at subduction zones (e.g., Chan et al. 1999; Nakano and Nakamura 2001; Chan et al. 2002; Bebout and Nakamura 2003; Zack et al. 2003), mainly due to their incompatibilities during melting (Ryan and Langmuir 1987; Brenan et al. 1998a), high fluid-mobility (e.g., Seyfried et al. 1984; Bebout et al. 1993; Ryan and Langmuir 1993; Brenan et al. 1998b) and easy-fractionating stable isotopes at low temperature (Moriguti et al. 2004). Tourmaline, as a dominant carrier of boron and lithium, and found in many rock types (e.g., Henry and Dutrow 1996; Nakano and Nakamura 2001; Busigny and Bebout 2013), is an important mineral which gives particular information about the chemical evolution of materials in subduction zones (Nakano and Nakamura 2001; Bebout and Nakamura 2003; Moriguti et al. 2004; Ota et al. 2008a, b). Consequently, studying the stability of tourmaline is important to build a basis for assessing the depth in which boron is still incorporated in tourmaline at subduction zones and explaining the anomaly of boron isotopes in basaltic volcanic rocks (Moriguti et al. 2004). For a single synthetic tourmaline end-member, dravite decomposes at temperature 900 °C, 6–8 GPa, and at 3–5 GPa, >1000 °C (Krosse 1995; Werding and Schreyer 1996). In the presence of SiO_2, however, tourmaline decomposes between 4 and 4.5 GPa at 800 °C and between 4.5 and 5 GPa at 700 °C (Ota et al. 2008a).

In this paper, we have investigated the stability of a natural tourmaline sample at high pressures (up to ~18 GPa) and relatively low temperatures (up to 723 K) using an external-heating diamond anvil cell combined with in situ synchrotron radiation angle-dispersive X-ray diffraction. The purpose is to identify the stability of tourmaline at high pressure and relatively low temperature. Although tourmaline has been proved to be stable at pressures lower than 8 GPa at high temperatures (>700 °C) by previous studies (Krosse 1995; Werding and Schreyer 1996; Ota et al. 2008a), there has been no detailed study on its stabilities at high pressures and relatively low temperatures. Investigation of tourmaline at these *P–T* conditions is significant for its application in geosciences, since cold conditions within slabs still exist to preserve colder slab temperatures to greater depths, for instance, at the coldest part of an old and fast subducting slab which can retain a relatively low temperature (~700 K) to a depth of ~540 km according to Bina and Navrotsky (2000), because the thermal evolution of the slab is strongly affected by the rate and the age of the subducting slab (Kincaid and Sacks 1997). In addition, despite the geothermobarometric potential of tourmaline (van Hinsberg and Schumacher 2009), its thermodynamic data are still limited. Consequently, the thermoelastic property of tourmaline was obtained by fitting the experimental *P–V–T* data and compared with previous studies and then

discussed the possibility of tourmaline along with subducting slab into deeper Earth.

Sample and experimental methods

A natural tourmaline sample was collected from Pakistan. The pure tourmaline grains were grounded in an agate mortar for 4–6 h to obtain a fine powder (a few microns). We used conventional powder X-ray diffraction method to examine the ground powder, after being heated at 50 °C in a constant temperature furnace for 2 h to eliminate the absorbed water. The ambient X-ray diffraction data were collected using a D/Max-2200 diffractometer with a graphite crystal monochromator and CuKα radiation. The spectrum was indexed using the standard spectrum (JCPDS 71-0716), confirming the structure is trigonal and belong to the space group of *R*3 *m*. The data of conventional diffraction collected at ambient condition give the parameters $a = 15.823$ (6) Å, $c = 7.089$ (4) Å and $V = 1537.1$ (11)vÅ^3. Chemical analysis based on electron microprobe technique showed that this tourmaline sample is uvite-dominated with a chemical formula of $[(Ca_{0.86}Na_{0.11}\square_{0.03})Mg_3(Al_{0.86}Mg_{0.09}V_{0.02})_6(Si_6O_{18})(BO_3)_3(OH)_3F]$, and the water content is constrained to be 2.43 wt%, assuming the molar ratio of H:O to be 1:10 (e.g., Ye et al. 2015).

Pressures up to 18.4 GPa were generated by a modified Merrill–Bassett-type diamond anvil cell (DAC) equipped with two 500-μm culet-size diamond anvil. A rhenium gasket was pre-indented to a ~70 μm thickness before laser drilling of a 200-μm-diameter hole. The tourmaline sample powder was mixed with 1.0 wt% gold powder which was used as the pressure calibrant. The mixture of these two powders was slightly pressed to form a disk of ~25 μm thickness, and then, a piece of this disk about 100 μm in diameter was loaded into the sample chamber. The pressure-transmitting medium was a mixture of ethanol–methanol–water (16:3:1), and the equation of state of gold (pressure marker) served as the pressure calibration (Fei et al. 2007). Temperatures up to 723 K were generated by a resistance-heating system and measured by a NiCr–NiSi thermocouple which was attached to the diamond. The experimental setup and cell assembly were described in detail by Fan et al. (2010).

High-pressure and high-temperature angle-dispersive X-ray diffraction was performed in situ at the 4W2 beamline of the Beijing Synchrotron Radiation Facility (BSRF), and diffraction images were acquired on a MAR-345 detector. The incident X-ray beam was monochromatic with a wavelength of 0.6199 Å which was calibrated by scanning through the Mo metal K-absorption edge. The X-ray beam was focused to a beam size of 35 × 14 μm^2 FWHM by two mirrors in the Kirkpatrick–Baez configuration. The tilting and rotation of the detector relative to the X-ray beam were calibrated using cerium dioxide (CeO_2) powder as the diffraction standard, so did the distance between sample and detector. Diffraction patterns were integrated and treated using the Fit2D (Hammersley 1996) and EXPGUI/GSAS (Toby 2001; Larson and Von Dreele 2004). The unit cell parameters of the sample and the pressure calibrant (gold) were both achieved by reducing full diffraction patterns following the LeBail method (Le Bail et al. 1988), and a typical fitting of the full diffraction pattern at 14.8 GPa and 573 K was shown in Fig. 2.

Results and discussion

Equation of State at 300 K

No phase transition was observed throughout the whole range of pressure and temperature performed in this study based on the X-ray diffraction patterns (Fig. 3). The variations of the d-spacings with pressures are continuous, which can also prove that tourmaline is stable within this pressure and temperature range in this study (Fig. 4). Table 1 shows the unit cell parameters and volumes of tourmaline at various pressures and temperatures. We first fitted the pressure–volume data at 300 K with the third-order-Birch–Murnaghan (III-BM) EoS (Birch 1947) to obtain the isothermal bulk modulus and its pressure derivative:

$$P = (3/2)K_0\left[(V_0/V)^{7/3}(V_0/V)^{5/3}\right] \times \left\{1 + (3/4)(K_0'4)\left[(V_0/V)^{2/3}1\right]\right\} \quad (1)$$

where V_0, V, K_0 and K_0' are the zero-pressure volume, high-pressure volume, isothermal bulk modulus and its

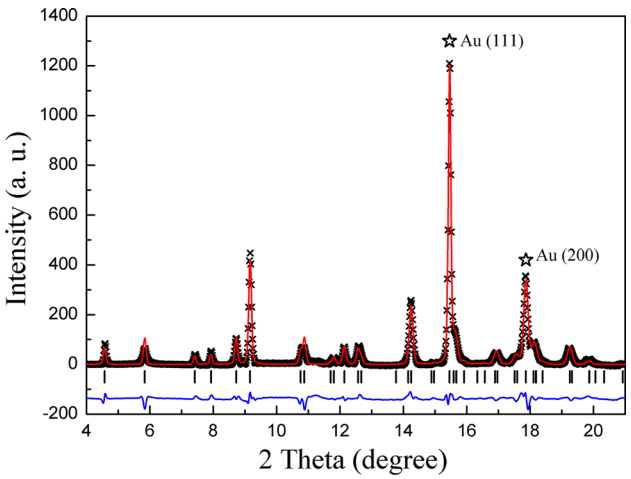

Fig. 2 Le Bail profile fitting of the diffraction profiles at 14.82 GPa and 573 K. Observed spectra (*black line*), fitted spectra (*red solid line*), difference plot (*blue solid line*) and Bragg peak positions (*tick marks*) are shown. (*Color online*)

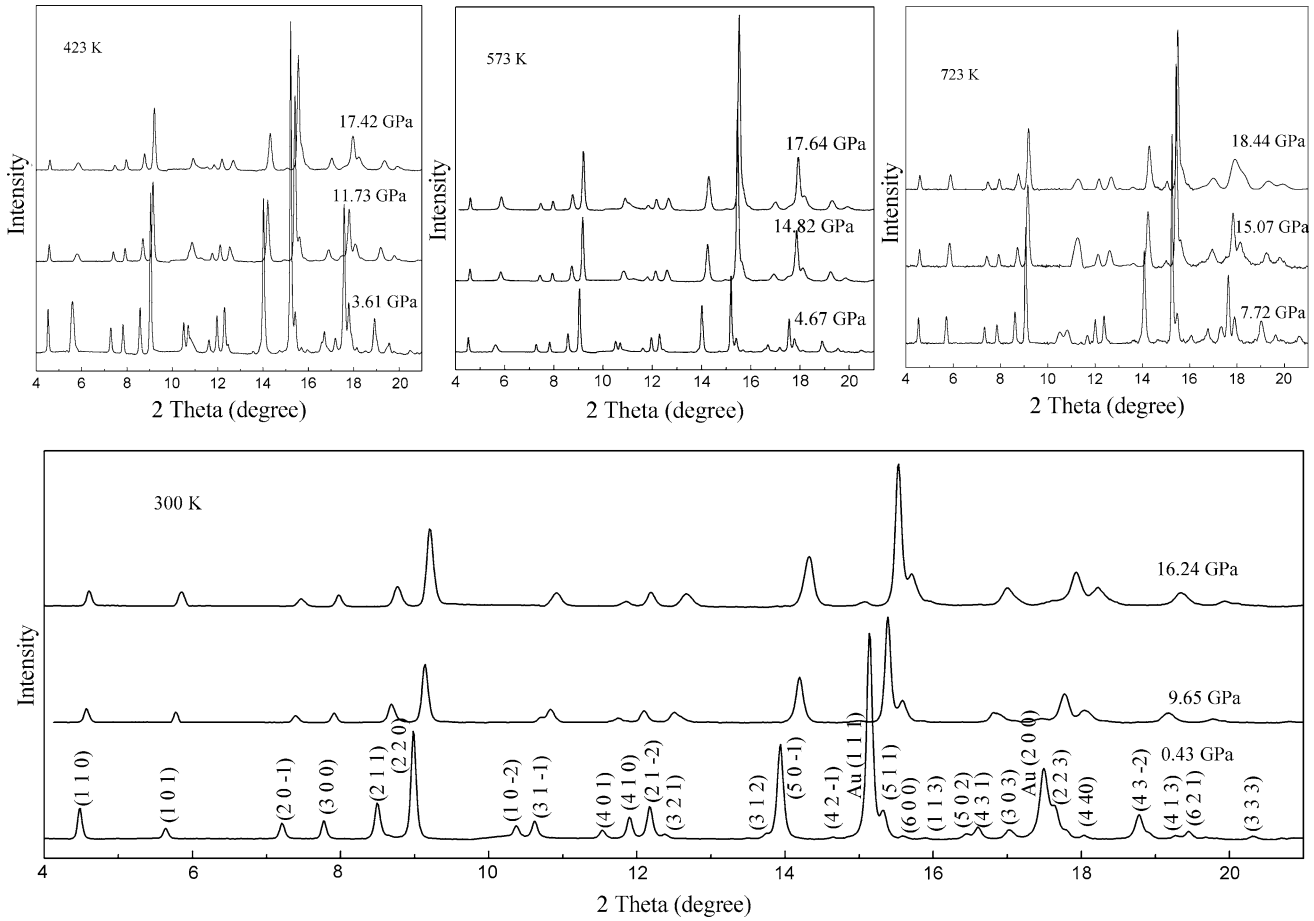

Fig. 3 Representative X-ray diffraction patterns of tourmaline obtained in this study at different pressures and temperatures of 300, 423, 573 and 723 K

pressure derivative, respectively. The least square fitting yielded $K_0 = 97$ (1) GPa, and $K_0' = 12.4$ (4). When fixing $K_0' = 4$, the isothermal bulk modulus was determined as 120 (2) GPa, respectively. The unit cell volume data at 300 K as a function of pressure and the compression curve calculated from these fitted parameters are shown in Fig. 5.

The evolution of the lattice parameters as a function of pressure exhibits a large anisotropy (Fig. 6). The lattice parameters were fitted to a linearized III-BM EoS (Angel 2000) to obtain the linear EoS parameters, yielding: $K_{a0} = 138$ (2) GPa and $K_{a0}' = 11.8$ (6) for the a-axis and $K_{c0} = 60$ (1) GPa and $K_{c0}' = 10.9$ (5) for the c-axis. We also calculated the axial compressibilities (with $\beta_d = 1/3K_0$, where K_0 is the isothermal bulk modulus at ambient conditions, β is the compressibility and d is the unit cell parameter) and obtained $\beta_a = 2.4 \times 10^{-3}$ GPa^{-1} and $\beta_c = 5.6 \times 10^{-3}$ GPa^{-1} for a- and c-axis, respectively. The elastic anisotropy can be expressed as: β_a: $\beta_c = 1.00$: 2.30.

Figure 7 shows the axial and volume Eulerian finite strain (for unit cell volume, $f_{EV} = [(V_0/V)^{2/3} - 1]/2$, and $f_{Ea} = [((a_0)^3/(a)^3)^{2/3} - 1]/2$ for lattice parameters) versus "normalized pressure" ($F_{EV} = P/[3f_{EV}(2f_{EV} + 1)^{5/2}]$, and $F_{Ea} = P/[3f_{Ea}(2f_{Ea} + 1)^{5/2}]$) plots [$f_E - F_E$ plot; (Angel 2000)]. The weighted linear fit of the data points yields the intercept values of F_{Ea} (0) = 135 (2) GPa for the a-axis, F_{Ec} (0) = 61 (1) GPa for the c-axis and F_{EV} (0) = 96.3 (8) GPa for the unit cell volume. It is clear from Fig. 7 that the data points lie on an inclined straight line with a relatively large positive slope, showing that the III-BM EoS is a reasonable description of the P–V data (e.g., Angel 2000; Burt et al. 2006; Nestola et al. 2010). Furthermore, the normalized stress values obtained at $f_E = 0$ are consistent with the axial and volume bulk moduli determined by the III-BM EoS.

The Vinet EoS (Vinet et al. 1986, 1987) was also used to analyze the P–V data at 300 K. The expression for the Vinet EoS is: $P(V) = 3K_0y^{-2}(1 - y)\exp[\eta_0(1 - y)]$, where $y = x^{1/3}$, $x = V/V_0$ and $\eta_0 = (3/2)(K_0' - 1)$. Analyses with all parameters free yield the values of $K_0 = 98$ (1) GPa and $K_0' = 11.3$ (3), which are close to that of $K_0 = 97$ (1) GPa, and $K_0' = 12.4$ (4) derived by the fitting to BM EoS within their uncertainties.

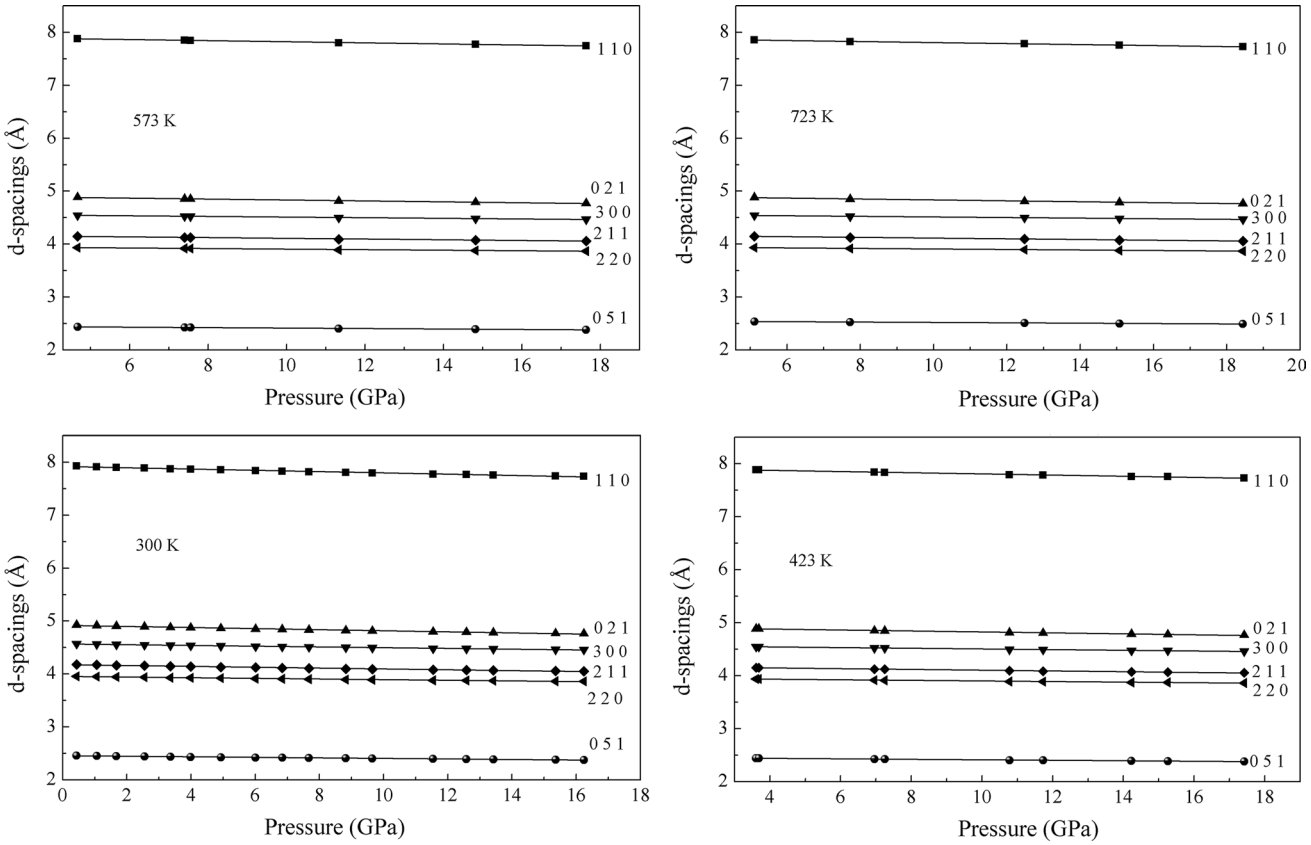

Fig. 4 Pressure dependence of the d-spacings of several crystallographic planes in tourmaline at temperatures of 300, 423, 573 and 723 K

High-temperature EoS

The high-temperature III-BM EoS:

$$P = (3/2)K_{T0}\left[(V_{T0}/V)^{7/3}(V_{T0}/V)^{5/3}\right] \times \left\{1 + (3/4)(K'_{T0}4)\left[(V_{T0}/V)^{2/3}1\right]\right\} \quad (2)$$

where K_{T0}, K'_{T0} and V_{T0} are bulk modulus, its pressure derivative and the unit cell volume at ambient pressure and temperature (in Kelvin), which was used to fit the *P–V–T* data in Table 1. V_{T0} (thermal dependences of the zero-pressure volume) and bulk modulus K_{T0} at different isotherms given by the following expressions:

$$V_{T0} = V_0 \exp \int_{300}^{T} \alpha_T \mathrm{d}T \quad (3)$$

$$K_{T0} = K_0 + (\partial K_{T0}/\partial_T)_P \times (T - 300) \quad (4)$$

where V_0, α_T and K_0 are the unit cell volume at ambient conditions, thermal expansion at temperature and ambient pressure and values of bulk modulus at ambient conditions. Generally, thermal expansion shall be assumed to be a linear function of temperature ($\alpha_T = \alpha_0 + \alpha_1 T$) (e.g., Liu et al. 2014). However, in view of the relatively low-temperature range (~723 K) and the limited high-pressure and temperature data points in this study, it is difficult to obtain reasonable result of α_1 (Nishihara et al. 2003). Therefore, $(\partial K_{T0}/\partial_T)_P$ and α_T were assumed to be constant over the temperature range in this study (Nishihara et al. 2003). By doing so, using the console program, EosFit7c (Angel et al. 2014), we obtained: $K_0 = 96.6$ (9) GPa, $K'_0 = 12.5$ (4), $(\partial K/\partial T)_P = -0.009$ (6) GPa K^{-1} and $\alpha_0 = 4.39$ (27) $\times 10^{-5}$ K^{-1}. The values of bulk modulus K_0 and its derivative K'_0 determined here are in good agreement with that derived from fitting of *P–V* data at 300 K. Figure 5 shows the evolution of cell volume with pressure and temperature as well as the isotherms calculated using the thermoelastic parameters. In addition, we also applied a "linearized" III-BM EoS with the EosFit7c program to calculate the linear thermoelastic parameters of this tourmaline sample, and we obtained: $K_{a0} = 139$ (2) GPa, $K'_{a0} = 11.5$ (7) and $\alpha_{a0} = 1.00$ (11) $\times 10^{-5}$ K^{-1} for the *a*-axis and $K_{c0} = 59$ (1) GPa, $K'_{c0} = 11.4$ (5) and $\alpha_{c0} = 2.41$ (24) $\times 10^{-5}$ K^{-1} for the *c*-axis.

To estimate the impact of non-hydrostatic compression to the results of elastic parameters derived from EoS fit, we calculated the bulk modulus (K_0) and its pressure derivative

Table 1 Unit cell parameters of tourmaline at various *P–T* conditions

P (GPa)	*T* (K)	*a* (Å)	*c* (Å)	*V* (Å^3)
0.0001	300	15.823 (6)	7.089 (4)	1537.1 (11)
0.4 (0)	300	15.8073 (2)	7.0746 (3)	1530.89 (7)
1.1(1)	300	15.7834 (3)	7.0529 (4)	1521.61(9)
1.7 (1)	300	15.7606 (3)	7.0295 (4)	1512.17 (10)
2.6 (1)	300	15.7365 (3)	7.0054 (5)	1502.37 (11)
3.4 (2)	300	15.7070 (5)	6.9883 (7)	1493.11 (15)
4.0 (2)	300	15.6923 (5)	6.9706 (8)	1486.53 (19)
4.9 (3)	300	15.6677 (4)	6.9495 (9)	1477.39 (20)
6.0 (3)	300	15.6361 (5)	6.9273 (11)	1466.73 (24)
6.8 (3)	300	15.6178 (4)	6.9129 (8)	1460.24 (19)
7.7 (4)	300	15.5953 (4)	6.8970 (9)	1452.70 (20)
8.8 (4)	300	15.5668 (6)	6.8767 (11)	1443.13 (25)
9.7 (5)	300	15.5468 (8)	6.8596 (11)	1435.86 (25)
11.5 (6)	300	15.5072 (6)	6.8339 (12)	1423.19 (26)
12.6 (6)	300	15.4899 (7)	6.8191 (15)	1416.96 (33)
13.4 (7)	300	15.4692 (7)	6.8085 (14)	1410.97 (32)
15.4 (8)	300	15.4403 (7)	6.7826 (18)	1400.40 (40)
16.2 (8)	300	15.4296 (12)	6.7666 (27)	1395.10 (60)
3.6 (2)	423	15.7250 (4)	6.9924 (5)	1497.40 (12)
3.7 (2)	423	15.7242 (4)	6.9921 (5)	1497.20 (12)
7.0 (4)	423	15.6371 (4)	6.9253 (7)	1466.51 (15)
7.3 (4)	423	15.6330 (5)	6.9190 (8)	1464.40 (18)
10.8 (5)	423	15.5415 (4)	6.8618 (8)	1435.33 (18)
11.7 (6)	423	15.5313 (7)	6.8394 (19)	1428.80 (40)
14.2 (7)	423	15.4724 (6)	6.8109 (11)	1412.04 (25)
15.3 (8)	423	15.4711 (6)	6.7911 (15)	1407.70 (32)
17.4 (9)	423	15.4245 (8)	6.7805 (19)	1397.10 (40)
4. 7 (2)	573	15.7183 (3)	6.9918 (5)	1496.00 (11)
7.4 (4)	573	15.6564 (5)	6.9278 (9)	1470.64 (19)
7.6 (4)	573	15.6468 (4)	6.9293 (7)	1469.15 (17)
11.3 (6)	573	15.5642 (7)	6.8625 (14)	1439.68 (30)
14.8 (7)	573	15.4986 (5)	6.8145 (12)	1417.59 (26)
17.6 (9)	573	15.4513 (6)	6.7842 (13)	1402.67 (29)
5.1 (3)	723	15.730 (3)	7.003 (6)	1500.7 (10)
7.7 (4)	723	15.676 (6)	6.934 (7)	1475.7 (14)
12.5 (6)	723	15.590 (6)	6.839 (7)	1439.5 (14)
15.1 (8)	723	15.522 (3)	6.823 (5)	1423.6 (8)
18.4 (9)	723	15.471 (3)	6.784 (5)	1406.2 (8)

(K_0') from fitting the *P–V* data within 10 GPa at room temperature and obtained: $K_0 = 97$ (1) GPa and $K_0' = 12.6$ (7), which is consistent with the results of fitting all room temperature data that lead to $K_0 = 97$ (1) GPa, and $K_0' = 12.4$ (4). Likewise, the thermoelastic parameters calculated from the *P–V–T* data within 10 GPa were also determined as: $K_0 = 96$ (1) GPa, $K_0' = 12.8$ (7), $(\partial K/\partial T)_P = -0.008$ (13) and $\alpha_0 = 4.35$ (49) $\times 10^{-5}$ K^{-1}, similarly, coincide with results from all *P–V–T* data [$K_0 = 96.6$ (9) GPa,

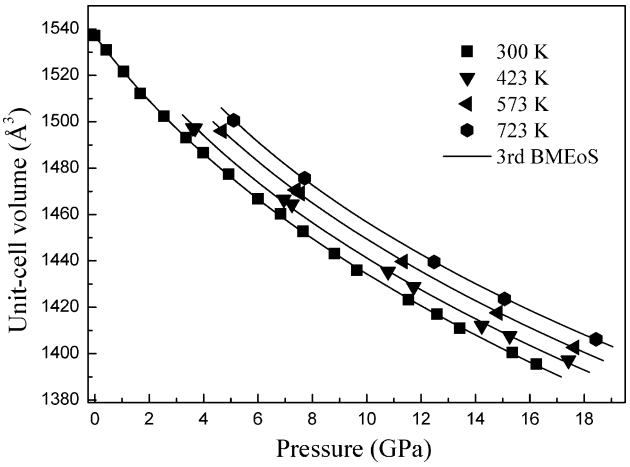

Fig. 5 Unit cell volume of tourmaline as a function of pressure and temperature. The *solid lines* represent isothermal compression curve calculated from thermoelastic parameters. The *error bars* of the data points are smaller than the *symbols*

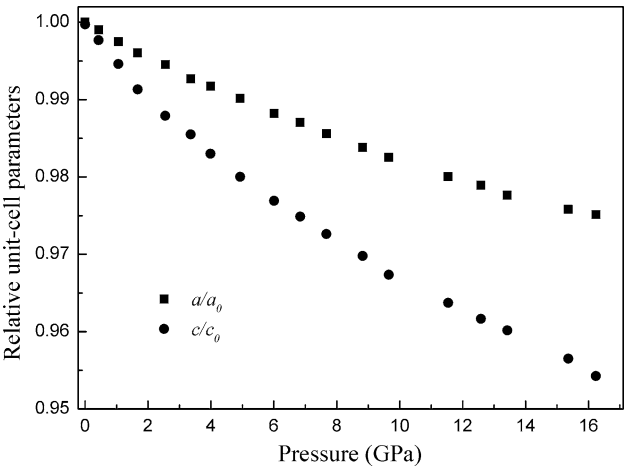

Fig. 6 Pressure dependence of the unit cell parameters *a* and *c* of tourmaline in this study. Note that the *symbols* are larger than the uncertainties

$K_0' = 12.5$ (4), $(\partial K/\partial T)_P = -0.009$ (6) and $\alpha_0 = 4.39$ (27) $\times 10^{-5}$ K^{-1}]. Therefore, the influence of non-hydrostatic stress on the thermoelastic parameters is limited in this study.

Cation effects on the compressibility

Schorl is another tourmaline species with Na^+, Fe^{2+} and Al^{3+} occupying *X*, *Y* and *Z* site, respectively, and its compressional property was examined by Li et al. (2004) using powder X-ray diffraction method in a DAC at high pressure (up to 27.8 GPa) and room temperature; they obtained the isothermal bulk modulus [$K_0 = 183.5$ (4.2) GPa] with K_0' constrained to be 4 (Table 2). In this study, the isothermal

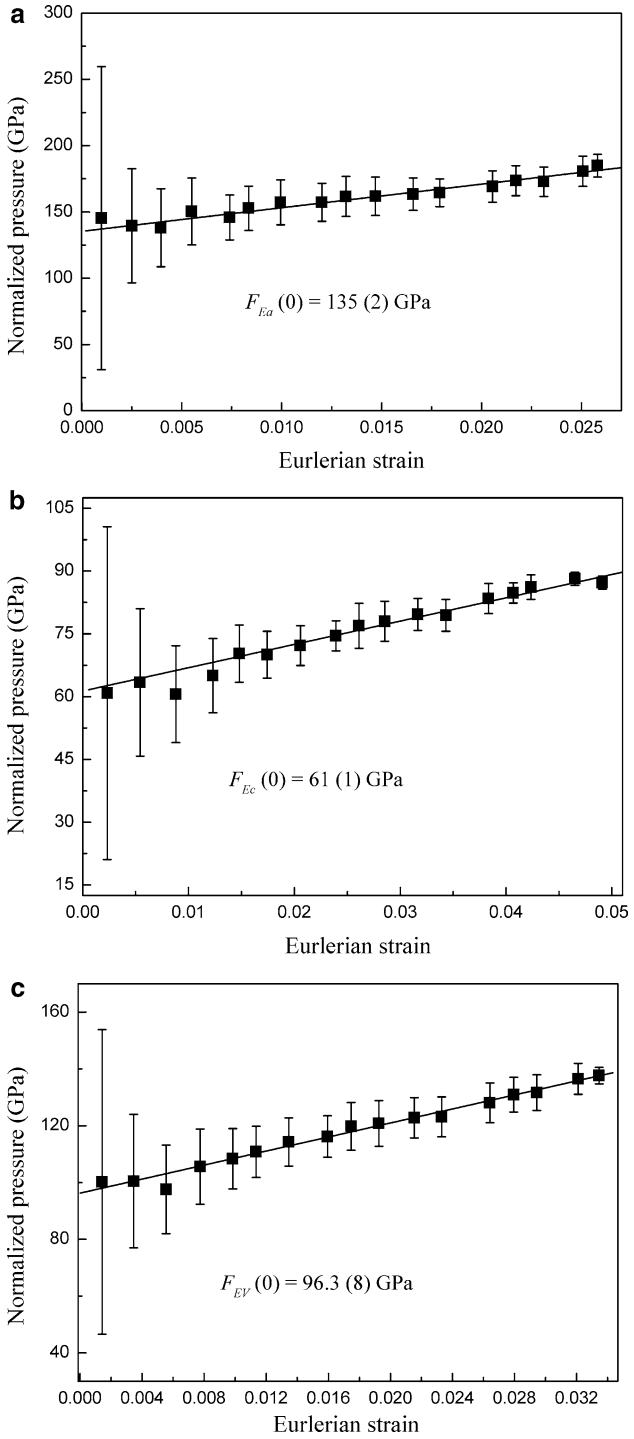

Fig. 7 Volume Eulerian strain-normalized pressure ($F_E - f_E$) plot of **a** *a* lattice parameter, **b** *c* lattice parameter and **c** unit cell volume. The *solid line* represents the linear fit through the data

bulk modulus of uvite [K_0 = 97 (1) GPa, K_0' = 12.4 (4), when fixing $K_0' = 4$, K_0 = 120 (2) GPa] is smaller than that of schorl. This difference could be explained by the compositional difference between them. The chemical analysis of this tourmaline sample showed that it is uvite-dominated [$(Ca_{0.86}Na_{0.11}\square_{0.03})Mg_3(Al_{0.86}Mg_{0.09}V_{0.02})_6(Si_6O_{18})(BO_3)_3(OH)_3F$] with *X*, *Y* and *Z* site mainly occupied by Ca^{2+}, Mg^{2+} and Al^{3+}. And that about 11 % of Na^+ and 3 % of vacancies exist in *X* site and *Z* site is also contains 9 % of Mg^{2+} and 2 % of V^{3+}. The effective ionic radius (IR) of Mg^{2+} (VI) ($IR_{Mg(VI)}$ = 0.72 Å) at *Y* site in uvite is close to that of Fe^{2+}($IR_{Fe(VI)}$ = 0.78 Å) in schorl (Shannon 1976) (Fe^{2+} is energetically favorable for the high spin state in silicates and oxides under ambient conditions (e.g., Lin and Tsuchiya 2008), so we selected the $IR_{Fe(VI)}$ of high spin state); however, at the *Z* site 9 % of $Mg^{2+}$and 2 % of V^{3+} substitute part of Al^{3+}, both of Mg^{2+} and V^{3+} have much larger IRs ($IR_{Mg(VI)}$ = 0.720 Å and $IR_{V(VI)}$ = 0.640 Å) than that of Al^{3+} ($IR_{Al(VI)}$ = 0.535 Å) (Shannon 1976), which likely results in a smaller isothermal bulk modulus of uvite than that of schorl. In addition, vacancies in *X* site would be also a possible attribution to the larger compressibility of uvite. A dravite-dominated sample [$NaMg_3Al_6(Si_6O_{18})(BO_3)_3(OH)_3OH$], which is generally occurred in subduction zone settings, has Al^{3+} mainly on Z site, possibly has a larger isothermal bulk modulus than that of uvite since $IR_{Al(VI)}$ (0.535 Å) is smaller than $IR_{Mg(VI)}$ (0.720 Å) (Shannon 1976).

Additionally, Li et al. (2004) got the isothermal bulk modulus value of schorl with K_0' fixed at 4; however, in this study of uvite-dominated tourmaline, we obtained that K_0 = 97 (1) GPa and K_0' = 12.4 (4) with free K_0', which indicates that fixing K_0' at 4 may be unreasonable to get a reliable value of K_0 for tourmaline group minerals because of the large dependence between isothermal bulk modulus (K_0) and its pressure derivative (K_0') (Bass et al. 1981). Consequently, this may be another reason for large difference (86.5 GPa) between K_0 values of schorl and uvite. Last, the data used to calculate the EoS parameters covered from 0 to 27.8 GPa (Li et al. 2004); however, the pressure-transmitting medium mixed by methanol, ethanol and water is non-hydrostatic at pressures more than about 10 GPa without heating (Angel et al. 2007). Hence, the K_0 value of schorl can be also influenced by the effect of non-hydrostatic stress. For this study of uvite, the impact of non-hydrostatic stress on the thermoelastic parameters was estimated to be limited which likely benefited from the heating during the experiment.

The K_0 value of the tourmaline sample in this study is much smaller than that of beryl ($[Al_2Be_3Si_6O_{18}]$, hexagonal, K_0 = 180 (1) GPa) and cordierite ($[Mg_2Al_3(AlSi_5)O_{18}]$, orthorhombic, K_0 = 131.0 (1.3) GPa) which belong to ring silicates group as well (Table 2). In the ring silicates group, the six corner-shared silicon tetrahedra ring is the basic structural building block. Beryl and cordierite have almost the same structure, but in cordierite structure one of the six tetrahedral site in the ring is occupied by Al^{3+} rather than Si^{4+}, and this reduces the symmetry (Nesse 2000). The smaller K_0

Table 2 Elastic parameters of tourmaline and other ring silicates (beryl and cordierite)

Sample	V_0 (Å^3)	K_0 (GPa)	K_0'	Method	References
Schorl	1595.52 (1.98)	183.5 (4.2)	4 (fixed)	Powder XRD	Li et al. (2004)
Uvite	1537.1 (11)	96.6 (9)	12.5 (4)	Powder XRD	This study
		120 (2)	4 (fixed)		
Beryl	675.3 (2)	180 (1)	4.2 (fixed)	Powder XRD	Fan et al. (2015)
	675.63 (4)	179 (1)	3.7 (3)	Single XRD	Prencipe and Nestola (2005)
Cordierite	1551.97 (15)	131.0 (1.3)	−0.5 (0.4)	Single XRD	Miletich et al. (2014)

XRD X-ray diffraction

value of cordierite compared with that of beryl can be possibly explained by the larger metal cations (Mg^{2+} and Al^{3+}) in its structure; the reason is that lager metal cations may cause large compressibilities for similar structural minerals (e.g., Zhang and Reeder 1999; Gao et al. 2014). For cordierite and beryl, the substitutions of Mg^{2+} for Al^{3+} in octahedral sites and Al^{3+} instead of Be^{2+} in tetrahedral site may cause a smaller K_0 value of cordierite, because the IR of Mg ($_{VI}$) ($IR_{Mg(VI)} = 0.720$ Å) is larger than that of Al ($_{VI}$) ($IR_{Al(VI)} = 0.535$ Å) and the $IR_{Al(VI)}$ (0.39 Å) is also larger than $IR_{Be(VI)}$ (0.27 Å) (Shannon 1976). Compared with beryl and cordierite, the K_0 value of the uvite sample in this study is much smaller (Table 2): one of the reasons may be the much larger cations ($IR_{Na(VI)} = 1.24$ Å and $IR_{Ca(VI)} = 1.18$ Å) in uvite, and the other reason is that the tourmaline structure contains $[OH]^-$ group which can dramatically increase the compressibilities of minerals according to the previous studies (e.g., Lager et al. 2002; Smyth et al. 2005; Xu et al. 2014, 2015; Fan et al. 2013; Jacobsen 2006).

Axial anisotropy of compressibility and thermal expansion in ring silicates minerals

The axial compressibility of the uvite sample shows the behavior of the *c*-axis direction being comparably softer than the *a*- and *b*-axis direction (Fig. 6) with a description of $\beta_a = \beta_b = 2.4 \times 10^{-3}$ GPa^{-1} and $\beta_c = 5.6 \times 10^{-3}$ GPa^{-1}. Similar anisotropic compression behaviors have been reported for experimental investigations on beryl [$\beta_a = \beta_b = 1.59 \times 10^{-3}$ GPa^{-1} and $\beta_c = 2.36 \times 10^{-3}$ GPa^{-1}; Fan et al. (2015)] as well as cordierite [$\beta_a = \beta_b = 2.4 \times 10^{-3}$ GPa^{-1} and $\beta_c = 3.1 \times 10^{-3}$ GPa^{-1}; Miletich et al. (2014)]. All of three common species of the ring silicates show the compression anisotropy with $\beta_c > \beta_a = \beta_b$, which can be explained by their characteristic sixfold rings which ranging along the directions parallel to *c*-axis. In the structures of beryl and cordierite, variable amounts of H_2O and other large alkali ions like Na^+ can be contained in the center of the channels in the rings; likewise, for tourmaline, large ions (e.g., Na^+ and Ca^{2+}) are also located along the axis of the column formed by tetrahedral rings. Therefore, the more compressible *c*-axis may be caused by the water molecular and large ions along the *c*-axis. Comparing the β_a, β_b and β_c of these three ring silicates, we find that the values of β_a and β_b (2.4×10^{-3}, 1.59×10^{-3} and 2.4×10^{-3} GPa^{-1} for tourmaline in this study, beryl and cordierite, respectively) for three species are closer than that of β_c (5.7×10^{-3}, 2.36×10^{-3} and 3.1×10^{-3} GPa^{-1} for tourmaline, beryl and cordierite); possibly, the smaller K_0 value of tourmaline is mainly controlled by the compression of direction for the *c*-axis. The more compressible *c*-axis in tourmaline compared with beryl and cordierite may be caused by its larger amount of large ions.

Donnay (1977) measured the unit cell parameters of a elbaite sample by powder X-ray diffraction at room pressure and temperatures of 193 and 293 K, and the derived thermal expansion coefficient is 4.56×10^{-5} K^{-1}. Thus, the thermal expansion coefficient of the tourmaline sample in this study [4.39 (27) $\times 10^{-5}$ K^{-1}] is in agreement with the result from Donnay (1977) (Table 3). The thermal coefficients of tourmaline with different compositions reported by Tatli and Pavlovic (1988) (method of dilatometry) and Pandey and Schreuer (2012) (method of strain gauge), however, are much too small for significative comparisons with that derived by X-ray diffraction method (Table 3). Compared with this tourmaline sample, the thermal expansion coefficient of another ring silicate beryl [$\alpha_0 = 0.282$ (74) $\times 10^{-5}$ K^{-1}; Fan et al. (2015)] is more than 10 times smaller, and the temperature derivative of the bulk modulus is close within its uncertainty though (Table 3). The behavior of negative thermal expansion for the *c*-axis (Fan et al. 2015) in beryl but not in this tourmaline sample can be an explanation for its smaller thermal expansion coefficient. Similar to the compression anisotropy of the *a*-axis and *c*-axis for this tourmaline sample, the thermal expansion of these two axial directions are also anisotropic with that the value of α_{c0} is about 2.40 times larger than that of α_{a0} (Table 4). Against the anisotropic property of compression, the *c*-axis has a smaller isothermal bulk modulus but get a larger thermal expansion and the *a*-axis is less expansive. Interestingly, in this study of tourmaline the degrees of anisotropy for compression and thermal expansion (K_{a0}/K_{c0} and α_{c0}/α_{a0}) are very close (Table 4).

Table 3 Thermal expansion coefficients and temperature derivatives of the bulk moduli of tourmaline and beryl

Sample	$(\partial K/\partial T)_P$ (GPa K^{-1})	α_0 (10^{-5} K^{-1})	Method	References
Elbaite		1.68[a]	Strain gauge	Tatli and Pavlovic (1988)
Schorl		1.55[a]		
Uvite		1.47[a]		
Elbaite–schorl		1.77[a]	Dilatometry	Pandey and Schreuer (2012)
Elbaite–schorl		1.69[a]		
Elbaite–schorl		1.62[a]		
Schorl–dravite		1.46[a]		
Schorl–dravite		1.48[a]		
Elbaite		4.56	Powder XRD	Donnay (1977)
Uvite	−0.009 (6)	4.39 (27)	Powder XRD	This study
Beryl	−0.017 (4)	0.282 (74)	Powder XRD	Fan et al. (2015)

XRD X-ray diffraction

[a] Calculated from the linear expansion coefficients α_{a0} and α_{c0}

Table 4 Linear axial thermoelastic parameters of the tourmaline sample in this study

K_{a0} (GPa)	K'_{a0}	K_{c0} (GPa)	K'_{c0}	α_{a0} (10^{-5} K^{-1})	α_{c0} (10^{-5} K^{-1})	K_{a0}/K_{c0}	α_{c0}/α_{a0}	
138 (2)	11.8 (6)	60 (1)	10.9 (5)			2.288 (9)		+
139 (2)	11.5 (7)	59 (1)	11.4 (5)	1.00 (11)	2.41 (24)	2.339 (4)	2.396 (31)	※

+ Calculated from *P–V* data at 300 K; ※ calculated from all *P–V–T* data

Geochemical and geophysical implications

In previous studies, tourmaline has been proved to be stable at ultrahigh-pressure conditions based on petrologic and experimental investigations (e.g., Krosse 1995; Werding and Schreyer 1996; Von Goerne et al. 1999; Kawakami 2001; Ota et al. 2008a; Dutrow and Henry 2011). In addition, the localized B isotope anomalies adjacent to convergent margins are possibly caused by tourmaline which carries B isotopes of sediments into deep mantle (Nakano and Nakamura 2001). For a single-phase, dravite [$NaMg_3Al_6(BO_3)Si_6O_{18}(OH)_4$] has been proved to be decomposed at temperatures larger than 1000 °C at 3–5 GPa, and 6–8 GPa at 900 °C (Krosse 1995; Werding and Schreyer 1996), which suggest that tourmaline is stable from Earth's surface to the depth of subarc. Recently, Ota et al. (2008a) investigated the stability of tourmaline [$(Na_{0.79}Ca_{0.03}(Mg_{1.97}Fe0.58Al_{0.21})Al_6(BO_3)_3Si_{6.05}O_{18}(OH)_4$] in a metapelitic system under high pressure and high temperature and observed that tourmaline breaks down at pressures of 4.5–5 GPa at 700 °C and 4–4.5 GPa at 800 °C, thus concluding that tourmaline breaks down before reaching the depth of 150 km. In this study, however, stability of a uvite-dominated sample was studied at pressures up to ~18 GPa and temperatures up to 450 °C, which implied that tourmaline may be stable under higher pressures than that of previous studies (Krosse 1995; Werding and Schreyer 1996) at relatively low temperatures (Fig. 8). This study suggests that tourmaline could be stable in a greater depth of

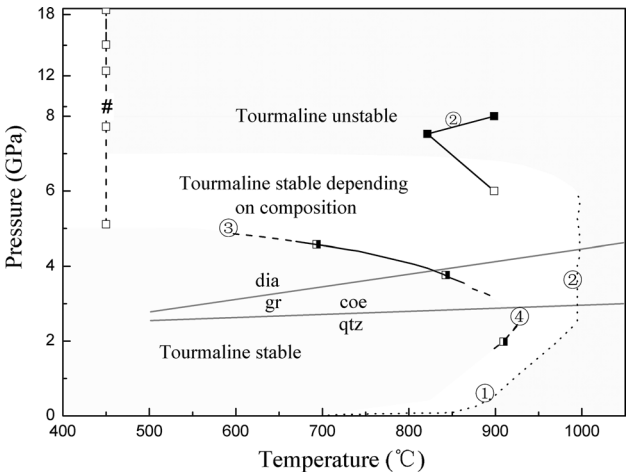

Fig. 8 *P–T* stability estimates for tourmaline of various compositions based on constrained from natural samples (*circle*) and experimental data (*squares*), with extrapolations (*dashed lines*). Selected reaction boundaries (*gray lines*) are shown for reference. Dravite: (*1*) Robbins and Yoder (1962); (*2*) Krosse (1995); (*3*) Ota et al. (2008a, b). Magnesio-foitite: (*4*) Werding and Schreyer (1996). Uvite: (#) This study. (*Note that this picture is drawn according to* "Fig. 3" *from* Dutrow and Henry 2011). *dia* diamond, *gr* graphite, *coe* coesite, *qtz* quartz

Earth's interior than previous estimates in relatively cold conditions such as subduction zones. Actually, such conditions may be exist in old and rapidly subducting slabs, for example, in northern Tonga where cold slab temperatures (about 700 K) could be preserved to a great depth

(~540 km) based on its subduction zone thermal model (Bina and Navrotsky 2000). However, no evidence that uvite and other tourmaline occur in subducted lithospheres so far, and temperatures at the surfaces of slabs are generally larger than that of interiors (e.g., Kincaid and Sacks 1997; Poli and Schmidt 2002), both are not beneficial for transporting tourmaline into deep Earth along with subducting slabs. Consequently, this study of the *P–T* stability of natural uvite-dominated tourmaline sample cannot be a direct proof that uvite or other tourmaline minerals can be transported into deep Earth (e.g., mantle) along with subducting slabs. Nonetheless, uvite-dominated tourmaline is stable in such a high pressures (up to 18 GPa) at relatively low temperatures (450 °C), which implies that tourmaline can possibly survive in deep-Earth conditions which occur in old and rapidly subducting slabs (like Tonga).

Conclusions

Using a modified Merrill–Bassett-type DAC coupled with synchrotron X-ray diffraction, we carried out the phase stability and *P–V–T* measurements on a natural tourmaline sample with the composition of uvite domination, at pressures between 0 and 18 GPa and temperatures up to 723 K. The thermoelastic properties of this sample have been derived by fitting the *P–V–T* data using high-temperature BM EoS and then obtained the zero-pressure volume, isothermal bulk modulus and its pressure derivative, thermal expansion coefficient and the temperature derivative of the bulk modulus. The axial moduli and thermal expansivities were also obtained by fitting a "linearized" BM EoS, which showed the anisotropic compression [$K_{a0} = 139$ (2) GPa and $K_{c0} = 59$ (1) GPa] and thermal expansion [$\alpha_{a0} = 1.00$ (11) $\times 10^{-5}$ K^{-1} and $\alpha_{c0} = 2.41$ (24) $\times 10^{-5}$ K^{-1}].

Acknowledgments This work is supported by the National Natural Science Foundation of China (Grant Nos. 41374107 and 41274105), and the Youth Innovative Technology Talents program of Institute of geochemistry, Chinese academy of Sciences (2013, to Dawei Fan). The experimental work was performed at 4W2 beamline of BSRF, which was supported by Chinese Academy of Sciences (Grant Nos. KJCX2-SW-N20 and KJCX2-SW-N03).

References

Angel RJ (2000) Equations of state. Rev Miner Geochem 41:35–59

Angel RJ, Bujak M, Zhao J, Gatta GD, Jacobsen SD (2007) Effective hydrostatic limits of pressure media for high-pressure crystallographic studies. J Appl Crystallogr 40:26–32

Angel RJ, Gonzalez-Platas J, Alvaro M (2014) Eosfit7c and a fortran module (library) for equation of state calculations. Zeitschrift für Kristallographie-Crystalline Materials 229:405–419

Bass JD, Liebermann RC, Weidner DJ, Finch SJ (1981) Elastic properties from acoustic and volume compression experiments. Phys Earth Planet Inter 25:140–158

Bebout GE, Nakamura E (2003) Record in metamorphic tourmalines of subduction-zone devolatilization and boron cycling. Geology 31:407–410

Bebout GE, Ryan JG, Leeman WP (1993) B-be systematics in subduction-related metamorphic rocks: characterization of the subducted component. Geochim Cosmochim Acta 57:2227–2237

Bina CR, Navrotsky A (2000) Possible presence of high-pressure ice in cold subducting slabs. Nature 408:844–847

Birch F (1947) Finite elastic strain of cubic crystals. Phys Rev 71:809–824

Brenan JM, Neroda E, Lundstrom CC, Shaw HF, Phinney FJ, Ryerson DL (1998a) Behaviour of boron, beryllium, and lithium during melting and crystallization: constraints from mineral-melt partitioning experiments. Geochim Cosmochim Acta 62:2129–2141

Brenan JM, Ryerson FJ, Shaw HF (1998b) The role of aqueous fluids in the slab-to-mantle transfer of boron, beryllium, and lithium during subduction: experiments and models. Geochim Cosmochim Acta 62:3337–3347

Burt JB, Ross NL, Angel RJ, Koch M (2006) Equations of state and structures of andalusiteto 9.8 GPa and sillimanite to 8.5 GPa. Am Miner 91:319–326

Busigny V, Bebout GE (2013) Nitrogen in the silicate earth: speciation and isotopic behavior during mineral-fluid interactions. Elements 9:353–358

Chan LH, Leeman WP, You CF (1999) Lithium isotopic composition of Central American volcanic arc lavas: implications for modification of subarc mantle by slab-derived fluids. Chem Geol 160:255–280

Chan LH, Leeman WP, You CF (2002) Lithium isotopic composition of Central American volcanic arc lavas: implications for modification of subarc mantle by slab-derived fluids: correction. Chem Geol 182:293–300

Desbois G, Ingrin J (2007) Anisotropy of hydrogen diffusion in tourmaline. Geochim Cosmochim Acta 71:5233–5243

Donnay G (1977) Structural mechanism of pyroelectricity in tourmaline. Acta Crystallogr A 33:927–932

Dutrow BL, Henry DJ (2011) Tourmaline: a geologic dvd. Elements 7:301–306

Fan D, Zhou W, Wei S, Liu Y, Ma M, Xie H (2010) A simple external resistance heating diamond anvil cell and its application for synchrotron radiation X-ray diffraction. Rev Sci Instrum 81:053903

Fan D, Wei S, Xie H (2013) An in situ high-pressure X-ray diffraction experiment on hydroxyapophyllite. Chin Phys B 22:010702

Fan D, Xu J, Kuang Y, Li X, Li Y, Xie H (2015) Compressibility and equation of state of beryl ($Be_3Al_2Si_6O_{18}$) by using a diamond anvil cell and in situ synchrotron X-ray diffraction. Phys Chem Miner 42:529–539

Fei Y, Ricolleau A, Frank M, Mibe K, Shen G, Prakapenka V (2007) Toward an internally consistent pressure scale. Proc Natl Acad Sci 104:9182–9186

Gao J, Zhu F, Lai XJ, Huang R, Qin S, Chen DL, Liu J, Zheng LR, Wu X (2014) Compressibility of a natural smithsonite $ZnCO_3$up to 50 GPa. High Press Res 34:89–99

Hammersley J (1996) Fit2d report. European Synchrotron Radiation Facility, Grenoble

Hawthorne FC, Dirlam DM (2011) Tourmaline the indicator mineral: from atomic arrangement to Viking navigation. Elements 7:307–312

Henry DJ, Dutrow BL (1996) Metamorphic tourmaline and its petrologic applications. In: Anovitz LM, Grew ES (eds) Boron: mineralogy, petrology and geochemistry, 33. Rev Mineral, Mineralogical Society of America, Chantilly, pp 503–557

Henry DJ, Kirkland BL, Kirkland DW (1999) Sector-zoned tourmaline from the cap rock of a salt dome. Eur J Miner 11:263–280

Henry DJ, Novák M, Hawthorne FC, Ertl A, Dutrow BL, Uher P, Pezzotta F (2011) Nomenclature of the tourmaline-supergroup minerals. Am Mineral 96:895–913

Hughes JM, Ertl A, Dya MD, Grew ES, Shearer CK, Yates MG, Guidotti CV (2000) Tetrahedrally coordinated boron in a tourmaline: Boron-rich olenite from Stoffhutte, Koralpe, Austria. Can Miner 38:861–868

Jacobsen SD (2006) Effect of water on the equation of state of nominally anhydrous minerals. Rev Miner Geochem 62:321–342

Jiang SY, Palmer MR, Yeats CJ (2002) Chemical and boron isotopic compositions of tourmaline from the archean big bell and mount gibson gold deposits, Murchison Province, Yilgarn Craton, Western Australia. Chem Geol 188:229–247

Kawakami T (2001) Tourmaline breakdown in the migmatite zone of the Ryoke metamorphic belt, SW Japan. J Metamorph Geol 19:61–75

Kincaid C, Sacks IS (1997) Thermal and dynamical evolution of the upper mantle in subduction zones. J Geophys Res 102:12295–12315

Krosse S (1995) Hochdrucksynthese, stabilität und eigenschaften der borsilikate dravit und kornerupin, sowie darstellung und stabilitätsverhalten eines neuen mg-al-borates. Unpublished Ph.D. thesis, Ruhr-Universität Bochum, 131 pp

Lager GA, Downs RT, Origlieri M, Garoutte R (2002) High-pressure single-crystal X-ray diffraction study of katoite hydrogarnet: evidence for a phase transition from Ia3d→ $I\bar{4}3d$ symmetry at 5 GPa. Am Mineral 87:642–647

Larson AC, Von Dreele RB (2004) General structure analysis system (GSAS). Los Alamos National Laboratory Report LAUR, pp 86–748

Le Bail A, Duroy H, Fourquet J (1988) Ab-initio structure determination of lisbwo6 by X-ray powder diffraction. Mater Res Bull 23:447–452

Lin JF, Tsuchiya T (2008) Spin transition of iron in the Earth's lower mantle. Phys Earth Planet Inter 170:248–259

Li H, Qin S, Zhu X, Liu J, Li X, Wu X, Wu Z (2004) In situ high-pressure X-ray diffraction of natural tourmaline. Nuclear Tech 27:919–922 **(in Chinese)**

Liu J, Lin JF, Mao Z, Prakapenka VB (2014) Thermal equation of state and spin transition of magnesiosiderite at high pressure and temperature. Am Miner 99:84–93

Marschall HR, Jiang SY (2011) Tourmaline isotopes: no element left behind. Elements 7:313–319

Marschall HR, Korsakov AV, Luvizotto GL, Nasdala L, Ludwig T (2009) On the occurrence and boron isotopic composition of tourmaline in (ultra)high-pressure metamorphic rocks. J Geol Soc Lond 166:811–823

Miletich R, Gatta GD, Willi T, Mirwald PW, Lotti P, Merlini M, Rotiroti N, Loerting T (2014) Cordierite under hydrostatic compression: anomalous elastic behavior as a precursor for a pressure-induced phase transition. Am Mineral 99:479–493

Moriguti T, Shibata T, Nakamura E (2004) Lithium, boron and lead isotope and trace element systematics of quaternary basaltic volcanic rocks in northeastern japan: mineralogical controls on slab-derived fluid composition. Chem Geol 212:81–100

Nakamura E, Campbell IH, Sun S (1985) The influence of subduction processes on the geochemistry of japanese alkaline basalts. Nature 316:55–58

Nakano T, Nakamura E (2001) Boron isotope geochemistry of metasedimentary rocks and tourmalines in a subduction zone metamorphic suite. Phys Earth Planet Inter 127:233–252

Nesse WD (2000) Introduction to mineralogy. Oxford University Press, New York

Nestola F, Ballaran TB, Angel RJ, Zhao J, Ohashi H (2010) High-pressure behavior of Ca/Na clinopyroxenes: the effect of divalent and trivalent 3d-transition elements. Am Miner 95:832–838

Nishihara Y, Takahashi E, Matsukage K, Kikegawa T (2003) Thermal equation of state of omphacite. Am Miner 88:80–86

Ota T, Kobayashi K, Katsura T, Nakamura E (2008a) Tourmaline breakdown in a pelitic system: implications for boron cycling through subduction zones. Contrib Mineral Petrol 155:19–32

Ota T, Kobayashi K, Kunihiro T, Nakamura E (2008b) Boron cycling by subducted lithosphere; insights from diamondiferous tourmaline from the kokchetav ultrahigh-pressure metamorphic belt. Geochim Cosmochim Acta 72:3531–3541

Palmer MR, Slack JF (1989) Boron isotopic composition of tourmaline from massive sulfide deposits and tourmalinites. Contrib Mineral Petrol 103:434–451

Pandey CS, Schreuer J (2012) Elastic and piezoelectric constants of tourmaline single crystals at non-ambient temperatures determined by resonant ultrasound spectroscopy. J Appl Phys 111:013516

Perfit MR, Gust DA, Bence AE, Arculus RJ, Taylor SR (1980) Chemical characteristics of island-arc basalts: implications for mantle sources. Chem Geol 30:227–256

Poli S, Schmidt MW (2002) Petrology of subducted slabs. Annu Rev Earth Planet Sci 30:207–235

Prencipe M, Nestola F (2005) Quantum-mechanical modeling of minerals at high pressure. The role of the Hamiltonian in a case study: the beryl ($Al_4Be_6Si_{12}O_{36}$). Phys Chem Miner 32:471–479

Robbins CR, Yoder HS (1962) Stability relations of dravite, a tourmaline. Carnegie Institute of Washington Yearbook 61:106–108

Rosenberg PE, Foit FF (1979) Synthesis and characterization of alkali-free tourmaline. Am Miner 64:180–186

Ryan JG, Langmuir CH (1987) The systematics of lithium abundances in young volcanic rocks. Geochim Cosmochim Acta 51:1727–1741

Ryan JG, Langmuir CH (1993) The systematics of boron abundances in young volcanic rocks. Geochim Cosmochim Acta 57:1489–1498

Saunders AD, Tarney J, Weaver SD (1980) Transverse geochemical variations across the Antarctic Peninsula: implications for the genesis of calc-alkaline magmas. Earth Planet Sci Lett 46:344–360

Schreyer W, Wodara U, Marler B, Seifert F, Robert JL (2000) Synthetic tourmaline (olenite) with excess boron replacing silicon in the tetrahedral site I. Synthesis conditions, chemical and spectroscopic evidence. Eur J Miner 12:529–541

Seyfried WE, Janecky DR, Mottl MJ (1984) Alteration of the oceanic crust: implications for geochemical cycles of lithium and boron. Geochim Cosmochim Acta 48:557–569

Shannon R (1976) Revised effective ionic radii and systematic studies of interatomic distances in halides and chalcogenides. Acta Cryst A 32:751–767

Slack JF (1996) Tourmaline associations with hydrothermal ore deposits. In: Grew ES, Anovitz LM (eds) Boron: mineralogy, petrology and geochemistry, vol 33 of Rev Mineral, 2nd edn., chap 11. Mineralogical Society of America, Washington, DC, pp 559–644

Slack JF, Trumbull RB (2011) Tourmaline as a recorder of ore-forming processes. Elements 7:321–326

Smyth JR, Frost DJ, Nestola F (2005) Hydration of olivine and the earth's deep water cycle. Geochim Cosmochim Acta 69:A746

Tatli A, Pavlovic AS (1988) Thermal-expansion of tourmaline single-crystals from 80 to 300 k. Phys Rev B 38:10072–10074

Taylor RP, Ikingura JR, Fallick AE, Huang Y, Watkinson DH (1992) Stable isotope compositions of tourmalines from granites and related hydrothermal rocks of the Karagwe-Ankolean belt, northwest Tanzania. Chem Geol 94:215–227

Taylor BE, Palmer MR, Slack JF (1999) Mineralizing fluids in the kidd creek massive sulfide deposit, Ontario: evidence from oxygen, hydrogen, and boron isotopes in tourmaline. In: Hannington MD, Barrie CT (eds) The giant Kidd creek volcanogenic massive sulfide deposit, western Abitibi Subprovince, Canada. Economic Geology Monograph, pp 389–414

Toby BH (2001) Expgui, a graphical user interface for gsas. J Appl Crystallogr 34:210–213

van Hinsberg VJ, Schumacher JC (2009) The geothermobarometric potential of tourmaline, based on experimental and natural data. Am Mineral 94:761–770

van Hinsberg VJ, Henry DJ, Dutrow BL (2011a) Tourmaline as a petrologic forensic mineral: a unique recorder of its geologic past. Elements 7:327–332

van Hinsberg VJ, Henry DJ, Marschall HR (2011b) Tourmaline: an ideal indicator of its host environment. Can Miner 49:1–16

Vinet P, Ferrante J, Smith JR, Rose JH (1986) A universal equation of state for solids. J Phys C Solid State Phys 19:L467

Vinet P, Ferrante J, Rose JH, Smith JR (1987) Compressibility of solids. J Geophys Res 92:9319–9325

Von Goerne G, Franz G, Wirth R (1999) Hydrothermal synthesis of large dravite crystals by the chamber method. Eur J Miner 11:1061–1077

Werding G, Schreyer W (1996) Experimental studies on borosilicates and selected borates. In: Grew ES, Anovitz LM (eds) Boron: mineralogy, petrology and geochemistry in the earth's crust. Rev Mineral 33:117–163

Wunder B, Berryman E, Plessen B, Rhede D, Koch-Mueller M, Heinrich W (2015) Synthetic and natural ammonium-bearing tourmaline. Am Mineral 100:250–256

Xu J, Ma M, Wei S, Hu X, Liu Y, Liu J, Fan D, Xie H (2014) Equation of state of adamite up to 11 GPa: a synchrotron X-ray diffraction study. Phys Chem Miner 41:547–554

Xu J, Kuang Y, Zhang B, Liu Y, Fan D, Zhou W, Xie H (2015) High-pressure study of azurite $Cu_3(CO_3)_2(OH)_2$ by synchrotron radiation X-ray diffraction and raman spectroscopy. Phys Chem Miner 41:805–816

Ye Y, Jacobsen SD, Mao Z, Duffy TS, Hirner SM, Smyth JR (2015) Crystal structure, thermal expansivity, and elasticity of OH-chondrodite: trends among dense hydrous magnesium silicates. Contrib Mineral Petrol 169:1–15

Zack T, Tomascak PB, Rudni RL, Dalpé C, McDonough WF (2003) Extremely light Li in orogenic eclogites: the role of isotope fractionation during dehydration in subducted oceanic crust. Earth Planet Sci Lett 208:279–290

Zhang J, Reeder RJ (1999) Comparative compressibilities of calcite-structure carbonates: deviations from empirical relations. Am Miner 84:861–870